Icarus 328 (2019) 152–159

Contents lists available at ScienceDirect

Icarus

journal homepage: www.elsevier.com/locate/icarus

Coronagraphic observations of the lunar sodium exosphere January–June, 2017

Rosemary M. Killen[a,*], Thomas H. Morgan[a], Andrew E. Potter[b], Claude Plymate[c], Roy Tucker[d], Jamil D. Johnson[e]

[a] NASA Goddard Space Flight Center, Solar System Exploration, Greenbelt, MD 20771, USA
[b] National Solar Observatory, Tucson, AZ 85719, Emeritus, USA
[c] Big Bear Solar Observatory, Big Bear Lake, CA 92314, USA
[d] Imaging Technology Laboratory, University of Arizona, Tucson, AZ 85721, USA
[e] Howard University, Dept. of Physics and Astronomy, Washington DC 20059, USA

ARTICLE INFO

Keywords:
Moon
Atmospheres, structure
Atmospheres, composition

ABSTRACT

In order to observe the lunar sodium exosphere out to one-half degree around the Moon, we designed, built and installed a small robotically controlled coronagraph at the Winer Observatory in Sonoita, Arizona. Observations are obtained remotely every available clear night from our home base at Goddard Space Flight Center or from Prescott, Arizona. We employ an Andover temperature-controlled 1.5 Å wide narrow-band filter centered on the sodium D_2 line, and a similar 1.5 Å filter centered blueward of the D_2 line by 3 Å for continuum observations. Our data encompass lunations in 2015, 2016, and 2017, thus we have a long baseline of sodium exospheric calibrated images. During the course of three years we have refined the observational sequence in many respects. Therefore this paper only presents the results of the spring, 2017, observing season. We present limb profiles from the south pole to the north pole for many lunar phases. Our data do not fit any power of cosine model as a function of lunar phase or with latitude. The extended Na exosphere has a characteristic temperature of about 2250–6750 K, indicative of a partially escaping exosphere. The hot escaping component may be indicative of a mixture of impact vaporization and a sputtered component.

1. Introduction

Sodium is only a trace element in the lunar exosphere, but of all the constituents in that exosphere, only sodium and potassium can be observed from Earth. The sodium emission is sufficiently intense that the spatial distribution can be observed at large distances about the Moon, typically greater than one lunar radius. Sodium can be seen in exospheres throughout the solar system, allowing inter-comparisons not possible with other atomic species. At least four mechanisms (sputtering, impact vaporization, thermal desorption, and photon-stimulated desorption) can eject this exospheric sodium from the surface, but their relative importance is not understood. The yield from two of these processes, sputtering and impact vaporization, depend on external fluxes: meteoroids, transient photon events, and transient ion events such as coronal mass ejections, plasma sheet crossings, and surface charging. The energy spectrum, and hence, the spatial distribution of sodium is different for each source process, thus observations along a single line of sight will not be definitive. The other important unknown is the surface interaction, including adsorption energy. A small set of observations obtained over a few observing runs cannot distinguish the importance of these processes in producing the sodium in the lunar exosphere. In addition to source processes, the loss through sticking is highly controversial. The variation with lunar phase can help to untangle these processes along with models.

Each mechanism proposed as a source for the lunar exosphere will produce ejecta characterized by a given temperature, spatial distribution and temporal variability. The general characteristics of each process are:

- Thermal desorption, characterized by the temperature of the surface;
- Photon-stimulated desorption, characterized by a temperature about 1200 K with a dependence approximately on the cosine of the solar zenith angle;
- Ion-sputtering, characterized by a hot, non-thermal velocity distribution and a having cosine dependence on the angle of the surface

* Corresponding author at: NASA Goddard Space Flight Center, Planetary Magnetospheres Lab/Code 695, Greenbelt, MD 20771, USA.
E-mail address: rosemary.killen@nasa.gov (R.M. Killen).

https://doi.org/10.1016/j.icarus.2019.02.027
Received 26 March 2018; Received in revised form 24 January 2019; Accepted 22 February 2019
Available online 16 March 2019

element with respect to the solar wind normal and a possible temperature dependence; and
- Meteoroid impact vaporization, probably characterized by a Maxwellian distribution at 3000–5000 K, with a maximum at the planetary ram direction, varying with periodic meteor shower events and sporadic events.

Wide angle narrow-band imaging of the Moon's extended corona was pioneered by Mendillo et al. (e.g. Baumgardner and Mendillo, 2009; Mendillo and Baumgardner, 1995; Mendillo et al., 1997). The existence of an extended lunar atmosphere at full moon was found by Mendillo et al. (1999), while Potter and Morgan (1994) found a declining near-moon exosphere as the moon traverses the Earth's magnetospheric lobes. Our observations, including high altitude data and a long baseline, were designed to distinguish between source processes and loss processes that produce a low altitude exosphere and those that produce the extended corona. A long-term program of observations to study the Moon's exosphere at both low altitudes and simultaneously at extended distances is necessary to produce a data set with the temporal coverage required, during a period of increasing solar activity, with which the importance of each of these processes can be determined. The importance of transient or episodic events in the production of the exosphere, including meteoroids (Szalay and Horanyi, 2016), solar wind influx (Mendillo et al., 1999; Sarantos et al., 2010), plasma sheet crossings (Wilson et al., 2006) and transient ion events such as coronal mass ejections can only be determined with a dedicated instrument giving a long baseline of observations (e.g. Barbieri et al., 2002; Smith et al., 2001).

In the past, observing campaigns have been undertaken to investigate the importance of some of these processes (e.g., Sprague et al., 1998). Observations were taken during the Leonid meteor showers of 1997 (Hunten et al. 1998; Wilson et al., 1999), and the Perseid shower of 2009 (Berezhnoy et al., 2014) to test the importance of impact vaporization by meteors. Observations of the lunar exosphere both outside and inside the Earth's magnetosphere were used to determine the importance of solar wind sputtering (Potter et al., 2000). Potter and Morgan did a statistical study using many non-consecutive data sets spanning the period 1988–1993, including phases from quarter, gibbous to full moon. Sarantos et al. (2010) reanalyzed this work to remove effects due to different lunar phases, and to include available solar wind data where possible (Figs. 5 and 6). Sarantos et al. (2010) collected all published measurements of lunar sodium and used this collection to test the relative importance of PSD, particle sputtering, and meteoroid impact for production of the sodium exosphere.

2. Description of the instrument

The lunar coronagraph was custom-designed by Claude Plymate and Roy Tucker. We employ off-the-shelf software primarily designed for amateur astronomers. The coronagraph is attached to a 101 mm refracting telescope (Televue NPF-4056 NP-101 f/5.4 APO refractor) which is operated remotely using the SkyX™ Professional software from Software Bisque. Seven different possible occulting disks, including an open disk, are housed on a rotary stage. In addition we have a 1.5 Å bandpass filter centered at 588.995 Å purchased from Andover Corporation and a 1.5 Å offband filter centered 3 Å blueward of the onband filter. A linear stage is used to select filters. The wavelength position is maintained by heating the filters to 51 C onband and 40 C offband using a CryoCon heater. Our science camera is an Andor iKon - M912 512 × 512 pixel imaging CCD, and our guide camera is an Imaging Source DMK 22AUC03. Autoguiding with the SkyX™ autoguiding software is performed by centering the guider on a bright crater and locking on the image of the bright spot. The telescope and autoguider are operated using the SkyX™ Professional software from Software Bisque. Observations are performed using two different MaximDL™ software packages separately for the science camera and guide camera.

3. Data reduction

In order to extract the lunar sodium corona the sky must be photometric, free of clouds or cirrus. Therefore we have chosen ten of our best nights to publish. These were all obtained in the spring of 2017. Earlier observations, especially those taken during the first two years of our program, were plagued with difficulties, first with imperfect guiding and with difficulty of re-acquiring the Moon at exactly the same place after changing filter and disk settings. With the replacement of a filter wheel with a linear stage, the positions of on and off band observations, as well as occulted and open filter observations remain stable throughout the series of observations.

There were three ways to obtain off band observations, either using the off-band filter or by tilting the on-band filter or cooling the onband filter to move the bandpass. Because tilting the filter changed the light path which produced ghost images and dramatically changed the transmission as a function of radial distance from the center of the field of view, we abandoned that procedure. We used a Cryocon heater to maintain the filters at optimum temperatures of 51 °C for onband and 40 °C for offband observations. Heating the filter is necessary because the Na transmission of the filter is designed for parallel light whereas the light is converging at the position of our filter. The FWHM and transmission function were measured by the Andover Corporation in their lab, but the maximum transmission is temperature dependent. The temperature dependence of our filters was independently verified by Dr. Jeffrey Baumgardner in his lab. The bandpass was measured as a function of temperature as seen in our coronagraph using observations of a Na lamp.

3.1. Data reduction procedure

Flat fields were obtained for white light (LED) and for the Na filter positions. All exposures are first divided by the LED flat to remove variations in transmission across the field. The Na images were divided by the Na flat to correct for variation of Na transmission across the field. Exposures of 10 min are required to image the sodium corona at good signal to noise. Autoguiding is performed by locking onto a small bright crater each night. Following each onband-offband exposure pair, on- and off-band images of the lunar surface are collected by taking 0.5–1.0 s exposures with the open filter. The sodium is calibrated using the counts in the open Moon images and the Hapke bi-directional reflectance function (Hapke, 1984, 1986; Helfenstein and Veverka, 1987; Mouawad et al., 2011). We use both dark and bright Hapke parameters for comparison check using Mare and highlands, respectively. In order to obtain the sodium profile around the entire limb, the images are transformed using a polar transform with the ImageJ™ software. The profiles are extracted automatically using a code written in IRAF. Detailed information on the data reduction is given in Supplementary information. The dates of observation with the lunar phase are given in Table 1. The subsolar point is rotated by the phase angle from the center of the disk as seen by the observer on Earth. Full Moon is at phase zero, and New Moon is phase 180°, denoting the angle between the Sun, Earth and Moon.

We determined surface number density, scale height and total vertical column abundance averaged in ten degree increments of latitude off the limb of the Moon for each of these dates as detailed in the Supplementary information. A brief account is given here.

We wish to calibrate the sodium D_2 scattered light in terms of kiloRayleighs, and we use the signal from a test region on the Moon for this purpose. The average solar intensity incident on the Moon is ϕ photons/s/cm^2/ster/Å for the spectral region of the filter. The solar continuum is taken as $4\ \pi \times 5.5 \times 10^{13}$ photons cm^{-2} s^{-1} Å^{-1}. Multiplying this by the bandpass $\boldsymbol{w}$ Angstroms of the filter (1.5 Å) yields the solar flux $\phi\boldsymbol{w}$ incident on the Moon over the bandpass of the spectral

Table 1
Dates of observations, phase angle and waxing or waning phase.

Date	Phase	Waxing/ waning	Local time of limb (hr:min)	Sub-Earth latitude (deg)
April 5	73	Waxing	13:13	3.6
March 8	56	Waxing	14:16	5.
May 2	103	Waxing	11:08	6
May 1	117	Waxing	10:12	5
Feb 2	118	Waxing	10:08	5
March 20	82	Waning	11:30	−6.2
March 19	71	Waning	10:45	−6.5
June 17	84	Waning	11:30	+3
June 18	95.9	Waning	12:20	+4.2
April 16	53	Waning	9:45	−6
Feb. 21	113	Waning	13:30	−6
Feb. 22	124	Waning	14:15	−5

filter. Now, we choose a region in the bare Moon image to be our "standard candle", usually near the bright limb but away from a bright crater ray. We find the Hapke reflectivity, R, (Hapke, 1984, 1986) for this region by use of a Fortran code which yields an image of the Moon in units of Hapke reflectivity for any given phase angle and bright or dark parameters (Helfenstein and Veverka, 1987). The codes were written by Potter, Killen and Morgan independently for gibbous and crescent phases, and for bright and dark reflectance. The sunlight is scattered from the lunar surface into 4π steradians. Multiplication of all these factors yields the photon irradiance scattered to our coronagraph as $4\pi\phi \boldsymbol{w} R$.

The camera signal from the standard region on the Moon is I counts, produced in a time interval τ. Now we have that I/τ are the counts per second from the test region on the Moon. The ratio of the photon flux $4\pi\phi \boldsymbol{w} R$ to the lunar test counts per second I/τ is the calibration constant for the observation. Multiplication of the sodium D_2 corona signal in counts per second by this factor yields the sodium D_2 photon irradiance, which can be expressed as kiloRayleighs by dividing by 10^9.

After calibration, we have an image of the corona that represents irradiance integrated along the line of sight. We must determine the line of sight column density and the variation of this with solar zenith angle. The scale height given is a simple exponential fit to the logarithm of the intensity vs altitude. The actual distance of the base of the observed corona from the lunar surface is known because we have the observations of the lunar disk at the same place where our corona observations were taken. Fig. 1 shows an example of the reduced data and Fig. 2 shows a polar transform obtained using the ImageJ™ software.

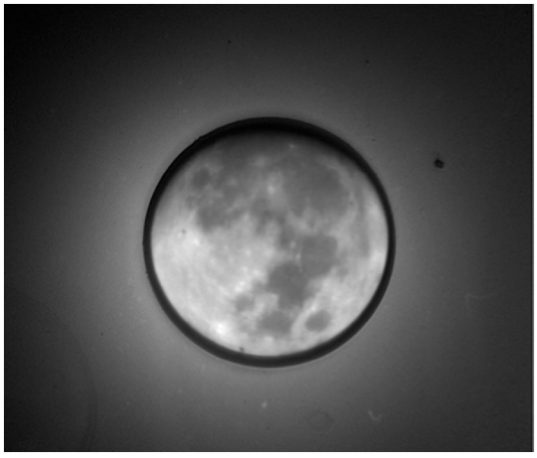

Fig. 1. Example of an observation of the Na corona (with occulting disk in place) and the unocculted Moon superimposed on the occulting disk. This image is not calibrated. The full Moon observation is taken either just before or just after the occulted image, and they are subsequently superimposed to determine the distance from the lunar limb to the occulting disk.

The images are rotated so that north is up before the polar transforms are taken. The data were sorted from south to north and separated into daytime and night-time files. Because of the orientation of the Moon, the waxing and waning phases required different sorting. The D_2 g-value (emission per atom per second) is taken to be 0.523 at the orbit of the Moon.

4. Results

We plotted intensity (Fig. 3), column abundance (Fig. 4), and scale height (Fig. 5), respectively, as a function of latitude. The results shown are all dayside observations. Our observations are shown as solid lines. The asterisks represent a cosine function in latitude scaled to the equatorial intensity. Waxing (Moon from new to full) and waning (Moon from full to new) phases are plotted separately. Table 1 gives the lunar phase, local time at the observed limb and the sub-Earth latitude for each observation.

Note that for waning phases the observer on Earth predominantly sees the dusk side of the Moon. However, the limb is on the dawn side for phase angles < 90° and on the dusk side for phase angles > 90°. For waxing phases the observer on Earth predominantly sees the dawn side of the Moon, but the limb is on the afternoon sector for phase angles < 90° and in the morning sector for phase angles > 90°. The largest scale heights correspond to the largest phase angles observed. Although the waxing phases more or less follow a trend with declining column abundance from morning to afternoon, the waning phases did not show a pattern with time of day.

5. Sources of uncertainty

Sources of uncertainty include changes in the sky conditions during the observation. We have discarded many observations where the sky was obviously or possibly unsteady during the course of the evening. The atmospheric transmission may also change as well as scattering due to cirrus or dust.

The estimation of the Hapke reflectivity is somewhat subjective. We have tried to avoid using the surface counts from crater rays or other unusually bright or dark regions. Perhaps the greatest source of error is the estimation of the light scatter into the onband filter from the continuum using the Full Moon data. This may introduce up to a 10% error due to a difference in sky conditions between the two dates of observation.

To measure the error in sodium level introduced by error in the ratio factor used to correct the 40 C image for subtraction from the 52 C image we analyzed six observations from near full Moon (phase angles ranging from 9 to 5°) to determine the ratio of 52 C images to 40 C images. The ratio was not a constant value over the whole field of view but was constant within a few percent over the range that lunar sodium was expected. For the five observations, the average ratio was 0.837 with a standard deviation of 0.010. To get a measure of the effect of that uncertainty on the lunar sodium levels, we used the observation set from 2017. For each observation pair (52 C and 40 C), we measured the maximum signal value, then corrected the 40 C value by the average ratio derived, and subtracted the result from the 52 C value. The difference represents a measure of the sodium emission intensity. We then repeated the calculation, now using the average ratio increased by the standard deviation. We calculated a percentage effect by subtracting the two sodium measures from one another, dividing by the uncorrected sodium value, and multiplying by 100. The results show that uncertainty in the basic 52C/40C ratio can result in uncertainties in the 5% range for phase angles greater than about 80°, with uncertainties increasing to levels of 15–20% at phase angles of 20% or less.

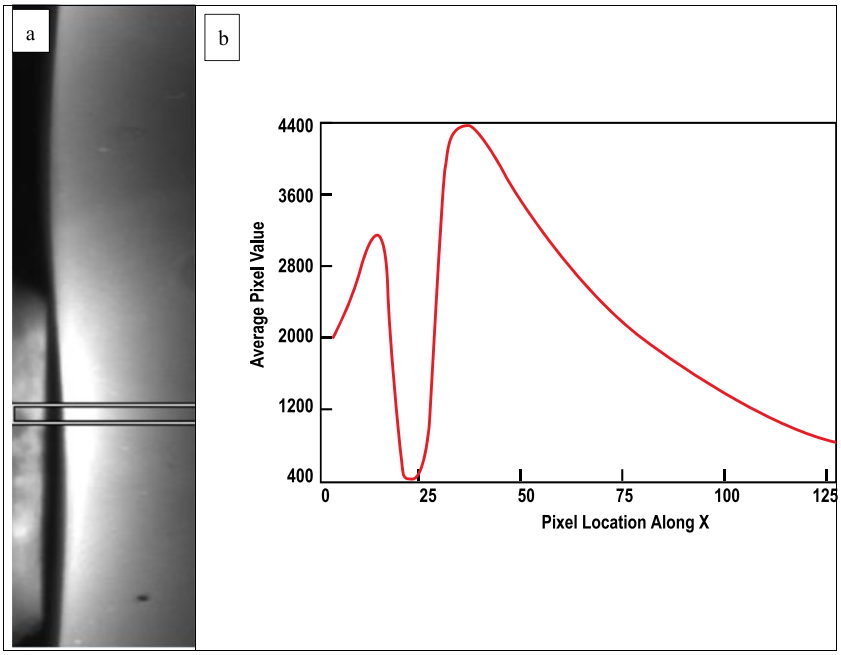

Fig. 2. An example of a polar transformed image from the ImageJ™ software (left). Horizontal scans are taken averaging 10 vertical pixels per scan. The data plotted at right show counts along x, vertically away from the Moon. The position of the lunar surface is known since the Moon is auto-tracked during the entire sequence and the overlaid open Moon and occulted Moon images are not shifted relative to each other. The counts are plotted on a log scale and extrapolated to the surface.

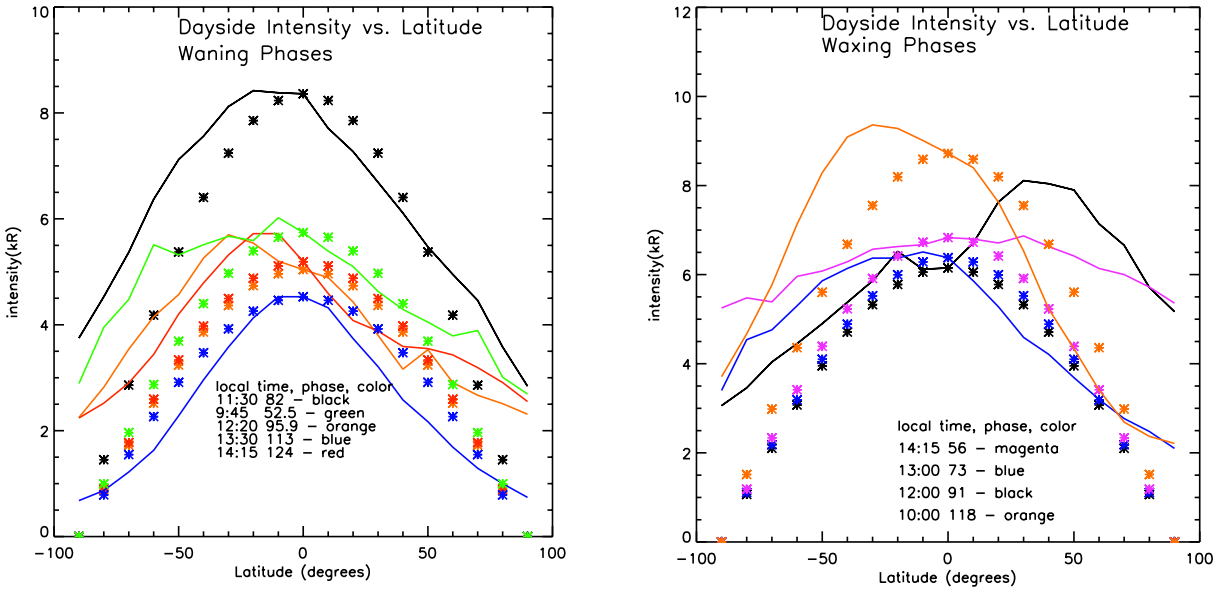

Fig. 3. Line of sight intensity (kR) at the surface as a function of latitude on the dayside for waning phases (left) and waxing phases (right). Waxing phases are observed from new Moon to full Moon, and waning from Full Moon to new Moon. A different pattern of Mare and Highlands is seen for each of these observations. Our observations are shown as solid lines. A cosine latitude function, normalized to the equatorial intensity at that date, is shown as asterisks with the same color as the corresponding date of observation. This shows that the data are not strictly symmetric about the equator nor do they follow a $\cos^2$ as expected from theory (e.g., Sarantos et al., 2010) or a $\cos^3$ functional form as found by Potter and Morgan (1998).

6. Discussion and conclusions

Most of our scale heights (Fig. 5) are on the order of 500–1500 km, at the equator increasing at high latitudes, compared with 320–388 km for comparable phase angles reported by Potter and Morgan (1988). Although a very cold component of the Na exosphere at about 140 K was reported by Stern and Flynn (1995), that component would be confined to altitudes below about 35 km from the surface, below the minimum altitude probed by our observations. Stern and Flynn (1995) reported exospheric temperatures increasing with latitude, consistent with our observations. Their derived temperature was > 3000 K for 80° latitude and a mixture of 1200 K and ~2500 K for low latitudes and above the very low altitudes where the cold Na would be observed. Potter and Morgan (1998) reported scale heights from 44 km (T = 191 K) at 70° N to 510 km (1736 K) at the equator measured at lunar phase 51°. Mendillo et al. (1993) reported scale heights for the extended Na exosphere that agree with ours: a sodium scale height of approximately 1000 km (T = 4500 K) near the equator increasing to 2000 km (T = 9000 K) at the poles.

Observations of the lunar sodium exosphere by Potter and Morgan (1998) at a lunar phase angle of 51° were reported to decrease as $\cos^3$ in latitude (Potter and Morgan 1998), with a characteristic temperature of about 1280 K, consistent with a photon-stimulated desorption source. Their scale heights were reported to decrease with latitude, in the opposite sense of our measured scale heights. One important difference between the Potter and Morgan (1998) observations and ours is that

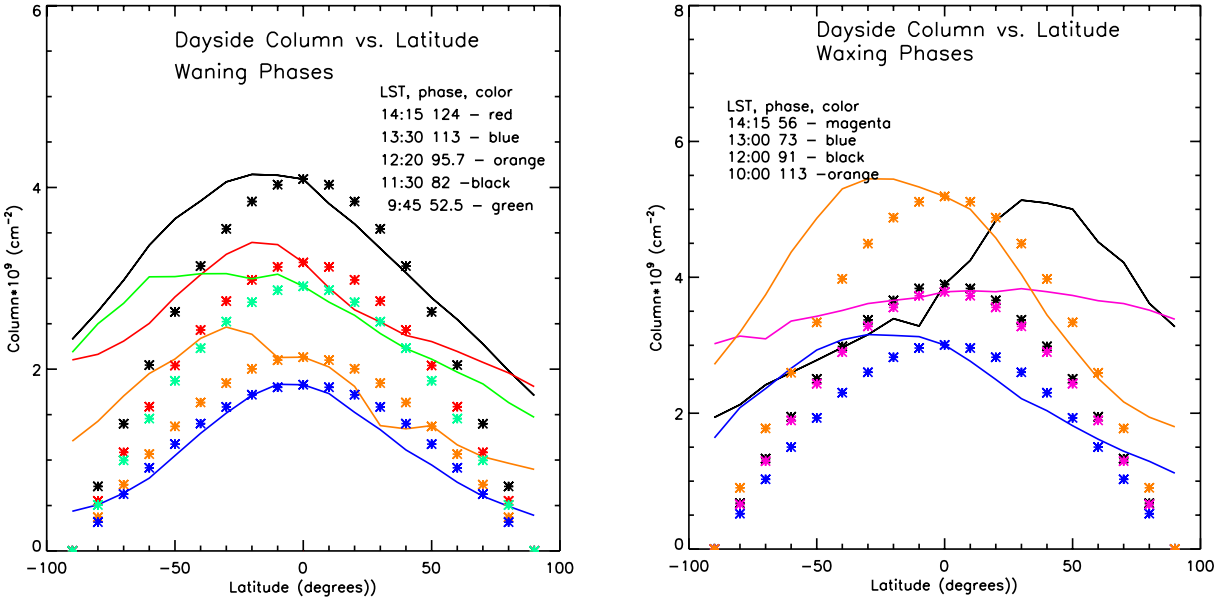

Fig. 4. Zenith column abundances from the surface for waning phases (left) and waxing phases (right). There is no obvious variation in column abundance with time of day. Column abundances at the equator vary from about $1.5 \times 10^9\,cm^{-2}$ to $\sim 5.5 \times 10^9\,cm^{-2}$.

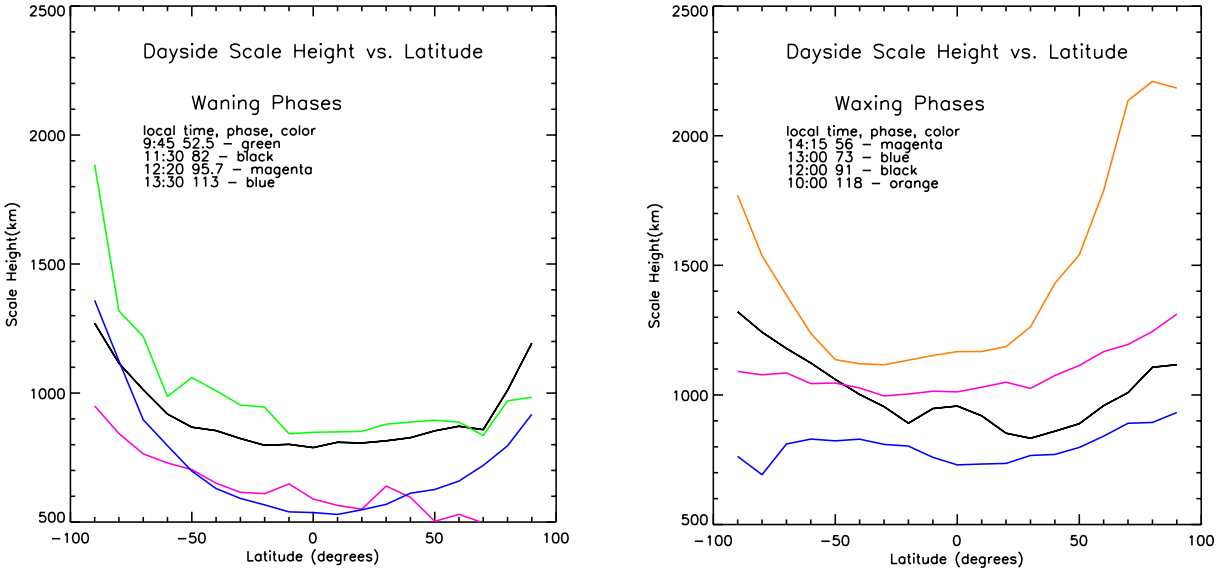

Fig. 5. Scale heights are shown on the right for waxing phases and on the left for waning phases 53, 82, 96, 113, 118. Most of the scale heights cluster between 500 and 1500 km increasing at higher latitudes. Scale heights appear to decrease from dawn to noon.

they used a 3 Å onband filter whereas we used a 1.5 Å bandpass; in addition they used a broad bandpass filter (50 Å) centered at 5860 Å for their off-band observation while we used a 1.5 Å bandpass filter centered at about 5996 Å. Therefore our scattered light correction is much more precise. Two of our observations have scale heights that agree with those published by Potter and Morgan (1998) at the equator. Our observations were obtained from approximately 143 km off the lunar surface to about one lunar radius above the surface, 1738 km. High resolution line profiles of lunar Na obtained with a Fabry-Perot spectrometer (Kuruppuaratchi et al., 2018) indicate a range of temperatures from 2500 K to 9000 K during magnetotail passages, with a systematic increase in temperature from quarter moon to full Moon. We do measure scale heights varying from roughly 500 to 1500 km (2255 K < T < 6765 K), consistent with Kuruppuaratchi et al. There is a definite increase in scale height for waning phases as the lunar phase decreases, but no monotonic trend is seen for waxing phases. Kuruppuaratchi et al. (2018) conclude that impact vaporization, sputtering and/or a non-thermal distribution for PSD likely combine to produce the trend that they show. Schmidt et al. (2018) presented evidence that the Na line profile observed in Mercury's exosphere increases with altitude. This may explain why some observers found a cold profile, while others concluded that the Na exosphere is hot. It is also possible that we observe the tail of an altitude profile derived from a non-thermal process.

The highly N/S asymmetric sodium profile seen at lunar phase 91 (Figs. 3 and 4) is consistent with observations published by Potter and Morgan (1991) where they report a D_2 emission intensity at an altitude of 50 km of ~0.45 kR at the west limb, 1.0 kR at the north limb, 2.0 kR at the south limb and 1.5 kR at the east limb, on Feb. 21, 1989. We often see N/S asymmetries of a factor of ~2, consistent with Potter and Morgan (1991).

Wilson et al. (2003) placed limits on the speed distribution required to match the distribution they measured at high altitudes. They

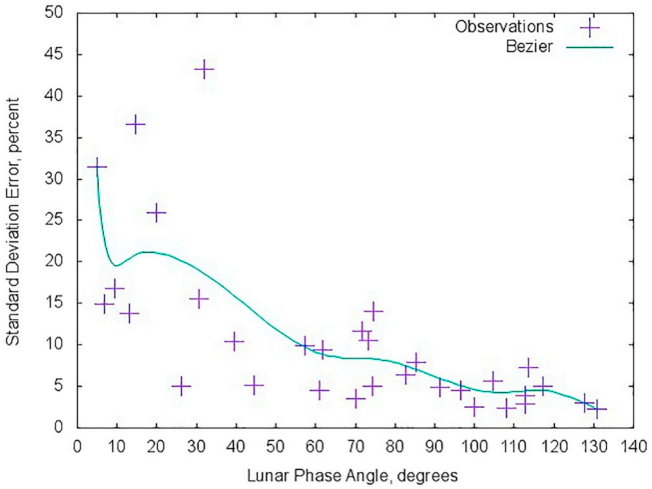

Fig. 6. Estimated error due to uncertainty in scattered light into the onband filter as a function of lunar phase angle. Because the error increases within 40° of full Moon we have not included those phases in our final results.

indicated that < 20% of the escaping Na atoms are ejected from the surface with speeds above 2.3 km/s and they concluded that solar radiation pressure is responsible for most of the neutral Na escape into the outer exosphere and Na tail. The fractional direct escape of Na from the Moon is about 20% for a Maxwellian distribution at 3000 K (Killen et al., 2017). This would indicate that our derived mean temperature of 4500 K may be the combination of an initial 3000 K distribution plus radiation pressure. Alternatively a portion of these escaping Na atoms may be due to sputtering. Given that the sodium ejected by impact vaporization may be expected to be colder than 4500 K, this temperature may indicate a mixture of impact vapor and sputter-derived sodium or the result of radiation pressure acceleration. Alternatively the derived high temperature may be the result of a mixture of a slightly cooler exosphere and an escaping component, given that half of the impact vapor released at 4500 K is on escaping trajectories which would not have a Chamberlain profile (Chamberlain, 1963) indicative of a bound component. Many of our waning phases peak at slightly southern latitudes, whereas some waxing phases peak at northern mid-latitudes. Scale heights appear to decrease from dawn to noon and increase from low to high latitudes.

It can be seen that the latitudinal variation we observed does not follow the $\cos^3(\psi)$, where ψ is the angle from the subsolar point, as reported by Potter and Morgan (1998). A cosine variation with lunar phase was reported by Potter and Morgan (1994), which was modeled by Sarantos et al. (2010). Our data do not fit any power of cosine model as a function of lunar phase or with latitude. Our data agree with the Potter and Morgan (1994) data for the same latitude and phase angles. For phase 69° Potter and Morgan (1994) reported Na emission of 5.53 kR at the equator and 2.01 kR at the south pole. We measured 6.79 kR extrapolated to the equatorial surface and 2.2 kR at the south pole. Our column abundance variation with latitude is more shallow than those reported by Potter and Morgan (1994) because our scale heights increase with latitude. Our data are much more consistent with the extremely high resolution spectroscopic observations obtained with the McMath-Pierce solar telescope published by Potter and Morgan (1994) in which they suggested that the source process is consistent with sputtering by solar wind particles. Potter and Morgan (1994) did not measure scale heights but our emission intensities are consistent for the phase angles we have both observed. We note that there is a scatter of more than an order of magnitude in sodium emission around the cosine model drawn in the Potter and Morgan (1994) paper, Fig. 1. For instance there is a variation of a factor of 7 in measured intensity at phase angle 100° in the Potter and Morgan (1994) Fig. 1. We see a variation of a factor of about 5 in emission at the equator between phases 53°–124°. When reduced to surface number density or column abundance the values are consistent with previous work. Because of the increased light scatter off the limb near full Moon, those results are not shown.

It is interesting that surface composition measurements taken by the Chandrayaan-1 X-ray spectrometer (C1XS) derived Na abundances of 2–3 wt% at mid-southern latitudes (Athiray et al., 2014), where we observed enhancements in the lunar Na exosphere. Colaprete et al. (2016) showed a strong correlation between the lunar potassium exosphere and surface K abundance, but the abundance variations in Na in the lunar regolith are poorly known. Our data are often slightly skewed to the south, therefore further measurements of surface composition are of interest.

We have not found any correlation with solar wind activity in these observations. We do not see any correlation with the sub-Earth latitude, which ranges ± 6°.

We cannot accurately report sodium emission at full Moon, even for the best conditions under which we have observed, because the expected Na irradiance is overwhelmed by the scattered light from the surface (Supplemental information). The expected Na emission at full Moon is about 3–5% of the total scattered light in the Na filter. The range of equatorial column abundances that we measured, $2–9 \times 10^9\,cm^{-2}$, is the same as that measured by the LADEE UV spectrometer (Colaprete et al., 2016); however, their measurement represents near equatorial noon at a range of lunar phase angles, whereas our measurements spanned a range of local times and the full range of latitude.

Observations of the lunar sodium exosphere were taken by the Kaguya spacecraft from an altitude of about 60 km looking antisunward from the nightside between December 2008, and June 2009 (Kagitani et al., 2010). They used a filter with a FWHM of 35 Å, and assumed temperatures of 2400 K and 6000 K to reduce the data to surface number density. They report a spherically symmetric exosphere that decreases from lunar phase 90° to phase 270°. We do not see such a trend but the observations we show here are dayside observations.

The LADEE sodium observations taken with the UVVS indicate that the exosphere peaks at full Moon. Those observations were taken on the dayside roughly subsolar whereas our observations are always taken at the limb. The observations indicate that the Moon's exosphere peaks at or near the sub-solar point at Full Moon, but the scale height appears to be minimum near noon.

Models are certainly required to determine physical effects such as radiation pressure, surface interaction, and the mixture of various source processes that affect the source, redistribution and loss of the lunar sodium. Note that observation down the tail (anti-sunward) is only seen at or near full moon which we cannot accurately observe. We can therefore make no conclusions regarding radiation pressure enhanced loss down the tail or the effect of the entrance or exit of the Moon from the Earth's magnetosphere as proposed by Sarantos et al. (2008).

Acknowledgements

RMK was supported by the DREAM2 Team of the NASA SSERVI Virtual Institute and by a NASA Grant from Solar Systems Observations. We thank Cassandra Hatcher for help with data reduction as a summer intern during 2016. We thank Mark and Pat Trueblood for their services and accommodations at the Winer Observatory. Jamil Johnson was a summer intern at NASA Goddard Space Flight Center in 2017 supported by the NASA Solar System Observations Program and the DREAM2 Team of NASA SSERVI. Roy Tucker selflessly traveled to the observatory to troubleshoot problems with the instrument.

Appendix A

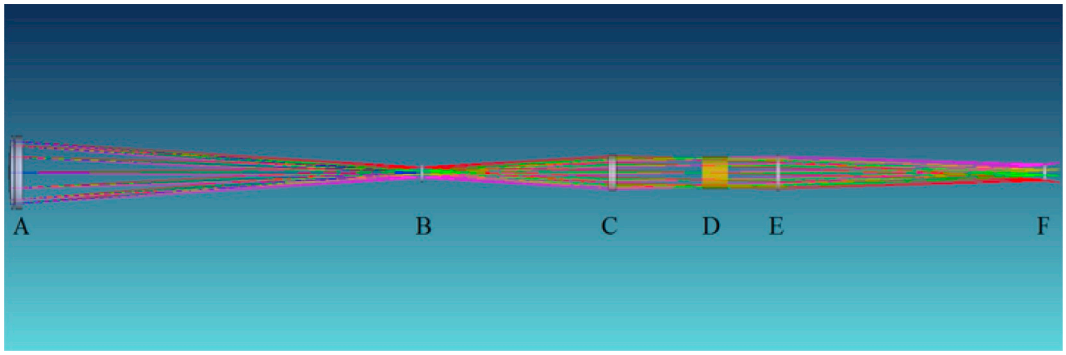

Fig. A1. Optical path for the coronagraph. A. Objective Lens; B. Field lens with occulting disk; C. Collimating lens; D. Filter; E. Reimaging lens F. CCD Detector.

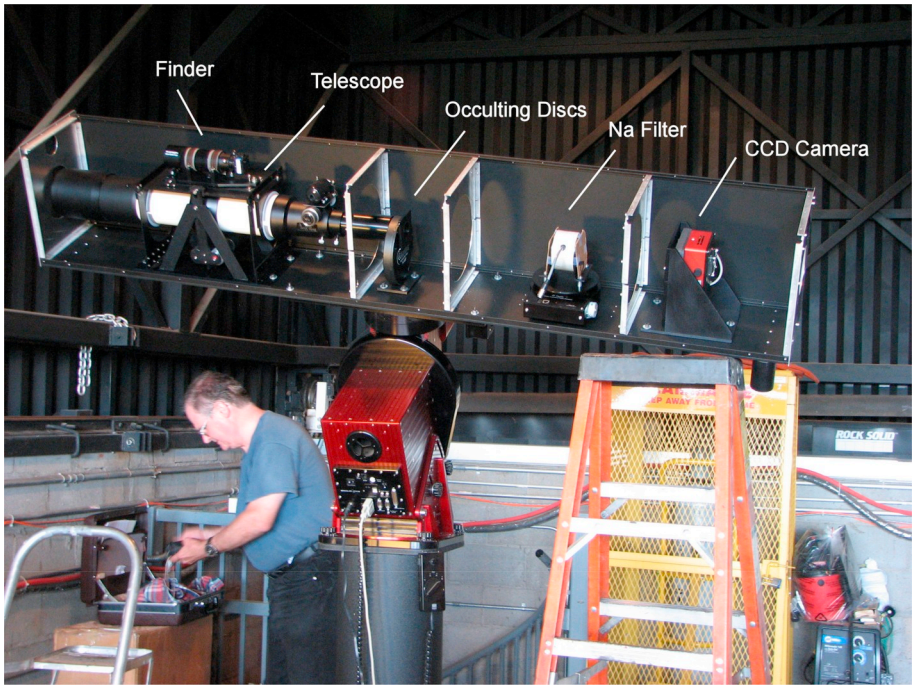

Fig. A2. Coronagraph with cover removed showing the layout. Roy Tucker is shown assembling the coronagraph.

Appendix B. Supplementary data

Supplementary data to this article can be found online at https://doi.org/10.1016/j.icarus.2019.02.027.

References

Athiray, P.S., Narendranath, S., Sreekumar, P., Grande, M., 2014. CIXS results-first measurement of enhanced sodium on the lunar surface. Planet. Space Sci. 104, 279–287.

Barbieri, C., et al., 2002. PLEXISS, a coronagraph for imaging the lunar atmosphere from the International Space Station. In: Fischer, Robert E., Smith, Warren J., Barry Johnson, R. (Eds.), Current Developments in Lens Design and Optical Engineering III. Proceedings of SPIE 4767. pp. 106–113.

Baumgardner, J., Mendillo, M., 2009. The use of small telescopes for spectral imaging of low-light-level extended atmospheres in the Solar System. Earth Moon Planet. 105, 107–113. https://doi.org/10.1007/s11038-009-9314-y.

Berezhnoy, A.A., Churyumov, K.I., Kleshchenok, V.V., et al., 2014. Properties of the lunar exosphere during the Perseid 2009 meteor shower. Planet. Space Sci. 96, 90–98.

Chamberlain, J.W., 1963. Planetary coronae and atmospheric evaporation. Planet. Space Sci. 11, 901–960.

Colaprete, A., Sarantos, M., Wooden, D.H., Stubbs, T.J., Cook, A.M., Shirley, M., 2016. How surface composition and meteoroid impacts mediate sodium and potassium in the lunar exosphere. Science 351, 249–252.

Hapke, B., 1984. Bidirectional reflectance spectroscopy. III - Correction for macroscopic roughness. Icarus 59, 41–59.

Hapke, B., 1986. Bidirectional reflectance spectroscopy. IV - The extinction coefficient and the opposition effect. Icarus 67, 264–280.

Helfenstein, P., Veverka, J., 1987. Photometric properties of lunar terrains derived from Hapke's equation. Icarus 72, 342–357.

Hunten, D.M., Cremonese, G., Sprague, A.L., Hill, R.E., Verani, S., Kozlowski, R.W.H., 1998. The Leonid meteor shower and the lunar sodium atmosphere. Icarus 136, 298–303.

Kagitani, M., Taguchi, M., Yamazaki, A., Yoshikawa, I., Murakami, G., Yoshioka, K., Kameda, S., Okano, S., 2010. Variation in lunar sodium exosphere measured from lunar orbiter SELENE (Kaguya). Planet. Space Sci. 58, 1660–1664.

Killen, R.M., Burger, M.H., Farrell, W.M., 2017. Exospheric Escape: a parametrical study. Adv. Space Res. https://doi.org/10.1016/j.asr.2017.06.015.

Kuruppuaratchi, D.C.P., Mierkiewicz, E.J., Oliversen, R.J., Sarantos, M., Derr, N.J., Gallant, M.A., Rosborough, S.A., Freer, C.W., Spalsbury, L.C., Gardner, D.D., Lupie, O.L., Roesler, F.L., 2018. High-resolution, ground-1 based observations of the lunar sodium exosphere during the LADEE mission. J. Geophys. Res. https://doi.org/10.

1029/2018JE005717.
Mendillo, M., Baumgardner, J., 1995. Constraints on the origin of the Moon's atmosphere from observations during a lunar eclipse. Nature 377, 404–406.
Mendillo, M., Flynn, B., Baumgardner, J., 1993. Imaging experiments to detect an extended sodium atmosphere on the Moon. Adv. Space Res. 13 (10), 313–319.
Mendillo, M., Emery, J., Flynn, B., 1997. Modeling the Moon's extended sodium cloud as a tool for investigating sources of transient atmospheres. Adv. Space Res. 19 (10), 1577–1586.
Mendillo, M., Baumgardner, J., Wilson, J., 1999. Observational test for the solar wind sputtering origin of the Moon's extended sodium atmosphere. Icarus 137, 13–23.
Mouawad, N., Burger, M.H., Killen, R.M., Potter, A.E., McClintock, W.E., Vervack, R.J., Bradley, E.T., Benna, M., Naidu, S., 2011. Constraints on Mercury's Na exosphere: combined MESSENGER and ground-based data. Icarus 211, 21–36. https://doi.org/10.1016/j.icarus.2010.10.019.
Potter, A.E., Morgan, T.H., 1988. Coronagraphic observations of the lunar sodium exosphere near the lunar surface. J. Geophys. Res. 103 (E4), 8581–8586 (Paper number 0148-0227/98/98JE-00059).
Potter, A.E., Morgan, T.H., 1991. Observations of the lunar sodium exosphere. Geophys. Res. Lett. 18 (11), 2089–2092.
Potter, A.E., Morgan, T.H., 1994. Variation of lunar sodium emission intensity with phase angle. Geophys. Res. Lett. 21, 2263–2266. https://doi.org/10.1029/94GL01702.
Potter, A.E., Killen, R.M., Morgan, T.H., 2000. Variation of lunar sodium during passage of the Moon through the earth's magnetotail. J. Geophys. Res. Planets 105, 15073–15084.
Sarantos, M., Killen, R.M., Sharma, A.S., Slavin, J.A., 2008. Influence of plasma ions on source rates for the lunar exosphere during passage through the Earth's magnetosphere. Geophys. Res. Lett. 35 (4). https://doi.org/10.1029/2007GL032310. CiteID L0410.
Sarantos, M., Killen, R.M., Sharma, A.S., Slavin, J.A., 2010. Sources of sodium in the lunar exosphere: modeling using ground-based observations of sodium emission and spacecraft data of the plasma. Icarus 205, 364–374. https://doi.org/10.1016/j.icarus.2009.07.039.
Schmidt, C., Baumgardner, J., Moore, L., Bida, T., 2018. Ground-based BepiColombo support with the rapid imaging planetary spectrograph. In: European Planetary Science Congress 16–21 September 2018, EPSC2018-1216.
Smith, S.M., Mendillo, M., Wilson, J.K., Baumgardner, J., 2001. Monitoring the Moon's transient atmosphere with an All-Sky-Imager. Adv. Space Res. 27, 1181–1187.
Sprague, A.L., Hunten, D.M., Kozlowski, R.W.H., Grosse, F.A., 1998. Observations of sodium in the lunar atmosphere during the international lunar atmosphere week, 1995. Icarus 131, 372–381.
Stern, S.A., Flynn, B.C., 1995. Narrow-field imaging of the lunar sodium exosphere. Astron. J. 109, 835–841.
Szalay, J.R., Horanyi, M., 2016. Annual variation and synodic modulation of the sporadic meteoroid flux to the Moon. Geophys. Res. Lett. 42. https://doi.org/10.1002/2015GL066908.
Wilson, J.K., Smith, J., Baumgardner, J., Mendillo, M., 1999. Modeling an enhancement of the lunar sodium atmosphere and tail during the Leonid Meteor Shower of 1998. Geophys. Res. Lett. 26, 1645–1648.
Wilson, J.K., Baumgardner, J., Mendillo, M., 2003. The outer limits of the lunar sodium exosphere. Geophys. Res. Lett. 30 (12), 1649. https://doi.org/10.1029/2003GL017443.
Wilson, J.K., Mendillo, M., Spence, H.E., 2006. Magnetospheric influence on the Moon's exosphere. J. Geophys. Res. 111 (A07207), 1–7.